Lecture 1: How to weigh a galaxy
Case study: B1938+666, AO vs. HST

Emilio E. Falco
Smithsonian Astrophysical Observatory
F. L. Whipple Observatory
670 Mt. Hopkins Rd.
Amado, AZ 85645, USA

Inspiration:

"A high-resolution multi-band view of the infra-red Einstein ring of JVAS B1938+666"
D. J. Lagattuta et al. 2012, MNRAS 424, 2800 (LAG12)

1. B1938+666

B1938+666 was found in the Jodrell Bank Very Large Array Astrometric Survey (JVAS; Patnaik et al. 1992; Browne et al. 1998; Wilkinson et al. 1998). Observations show a quadruply-imaged source forming arcs, as well as a second, doubly-imaged component (King et al. 1997) (Fig. 1).

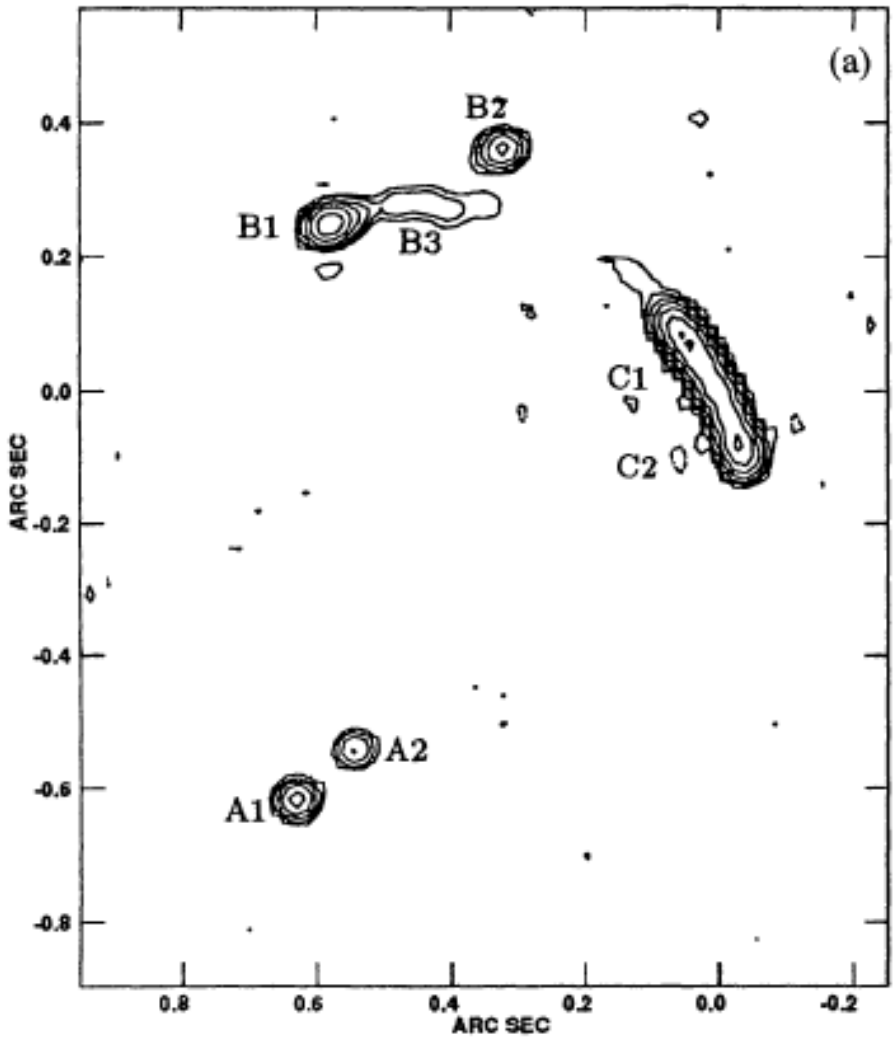

Fig. 1.— MERLIN 5 GHz map of B1938+666 (King et al. 1997). Restoring beam size 0.″04. Logarithmic contours; lowest 3σ contour is 0.5 mJy beam^{-1}.

Follow-up imaging at near-infrared (NIR) and optical wavelengths shows a bright red object that was thought to be the galaxy lensing the radio emission (Rhoads, Malhotra & Kundic 1996). However, later NIR HST images revealed emission from a lens galaxy and a complete Einstein ring (CASTLES, King et al. 1998; Fig. 2). Tonry & Kochanek (2000) measured a redshift of $z_l = 0.88$ for the lens galaxy with optical spectroscopy.

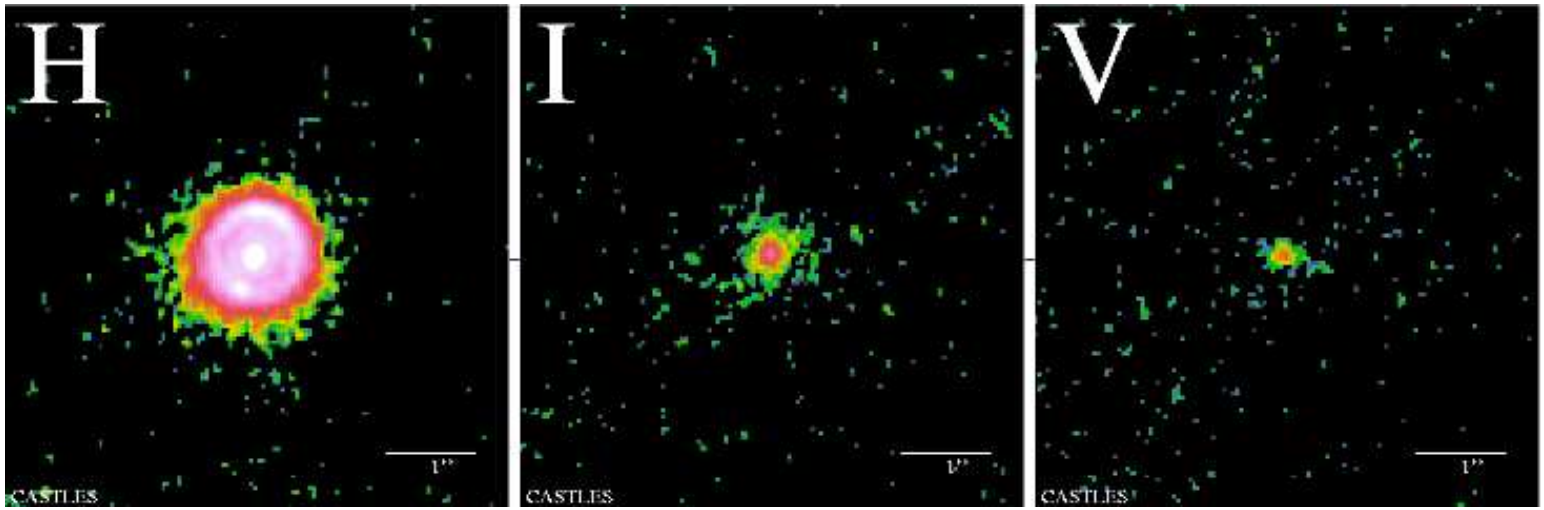

Fig. 2.— CASTLES Views show the lens galaxy is (barely) visible in V.

Riechers (2011) measured a redshift of $z_s = 2.06$ for the source from CO observations. Let us assume a concordance cosmological model, $H_0 = 100$ h km/s/Mpc, $\Omega_m = 0.3$, and $\Omega_\Lambda = 0.7$.

The source redshift was unknown at the time of the LAG12 observations. LAG12 obtained spectra of B1938+666 with the near-infrared echelle spectrograph (NIRSPEC; McLean et al. 1998) on the Keck- II telescope. They used the NIRSPEC-5 (roughly H-band) and NIRSPEC-7 (roughly K-band) filters. Their spectra are shown in Fig. 3. Thus, although LAG12 would not have been able to unambiguously measure the source redshift with the NIRSPEC spectra, their data are consistent with the redshift measured by Riechers (2011).

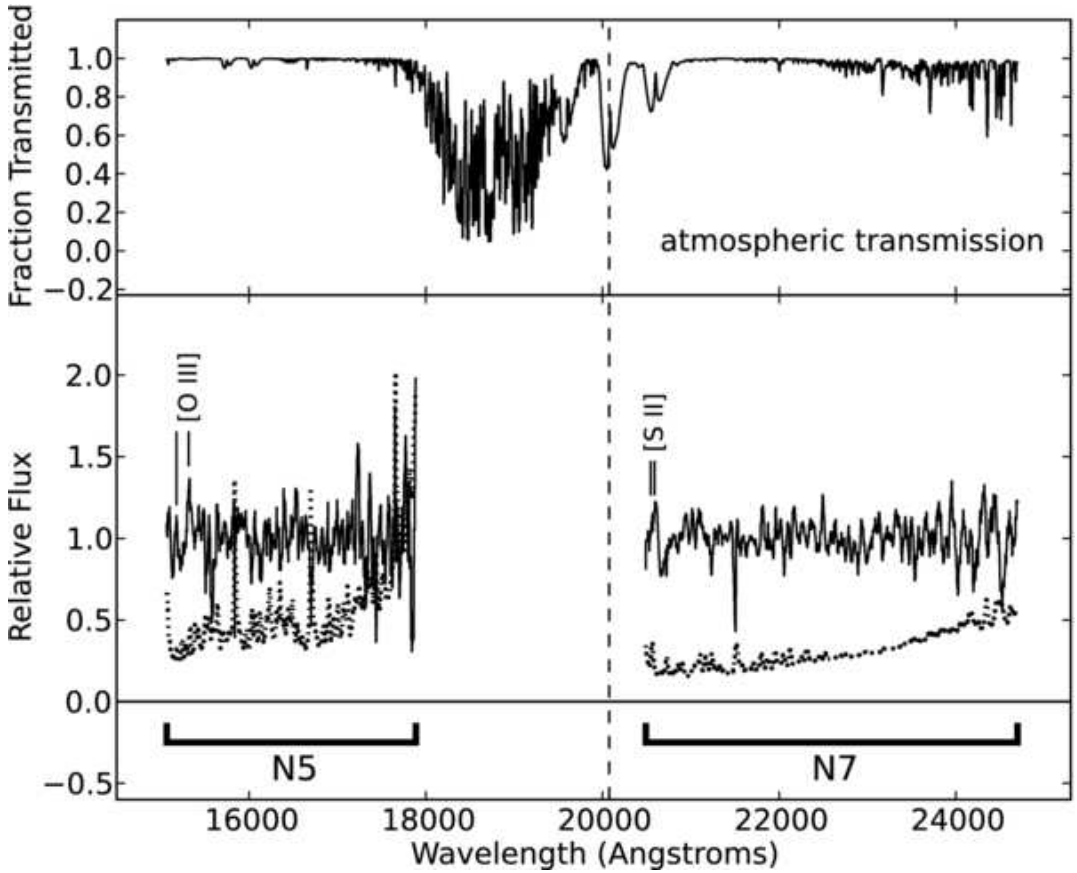

Fig. 3.— NIRSPEC spectra of the combined emission from the lens galaxy and background source (solid) and the 1σ error spectrum (dotted). Spectra are normalized and smoothed by a 9-pixel moving average, with inverse-variance weighting. The expected positions of the [O III] $\lambda\lambda 4959, 5007$and [S II] $\lambda\lambda 6716, 6731$lines at the background source redshift of z = 2.059 (Riechers 2011) are marked. The vertical dashed line is the expected position of Hα. The atmospheric transmission is in the upper panel.

2. GOALS

1. Obtain refined mass models, based on multi-wavelength Keck adaptive optics (AO) and HST data. The Strong-lensing at High Angular Resolution Program (SHARP) described in LAG12 plans to study quadruple-image and Einstein ring lenses using high-resolution imaging, to probe their light and dark mass distributions in new detail.

2. Analize the differences between AO-and HST-derived lens models: at least when the lens and source galaxies are both bright and red, and the system has a high degree of circular symmetry, AO-based models place significantly tighter constraints on model parameters.

3. Estimate the physical properties of the system: mass density slope of the lens galaxy γ, projected dark matter mass fraction within the Einstein radius M_{dark}/M_{lens}, total magnification factor of the source galaxy, set limits on luminous substructure.

4. Determine whether faint structure visible near the ring is lensed.

3. DARK MATTER

Measurements of the shapes of galaxies reveal the presence of dark matter (e.g., Rubin, Peterson, & Ford 1980; van Albada & Sancisi 1986; de Blok & McGaugh 1997; Bosma 1999; Gavazzi et al. 2007; Conroy et al. 2007; Dutton et al. 2011; Ruff et al. 2011) and its interaction with baryonic matter (e.g., Blumenthal et al. 1986; Gnedin et al. 2004; Auger et al. 2010; Schulz, Mandelbaum, & Padmanabhan 2010). Determinations of luminous and dark components yields constraints on cosmological parameters (e.g. the baryon fraction Ω_b) and estimates of the efficiency of star-formation in galaxies (e.g., Fukugita, Hogan, & Peebles 1998; Heymans et al. 2006; Napolitano, Romanowsky, & Tortora 2010; Lagattuta et al. 2010). Observations of changes in these quantities over cosmological time yield a view of galaxy evolution (e.g., Mandelbaum et al. 2006; Behroozi, Conroy, & Wechsler 2010; Lagattuta et al. 2010).

As an example, Suyu et al. (2012) disentangle baryons and dark matter in the complex gravitational lens system B1933+503 shown in Fig. 4.

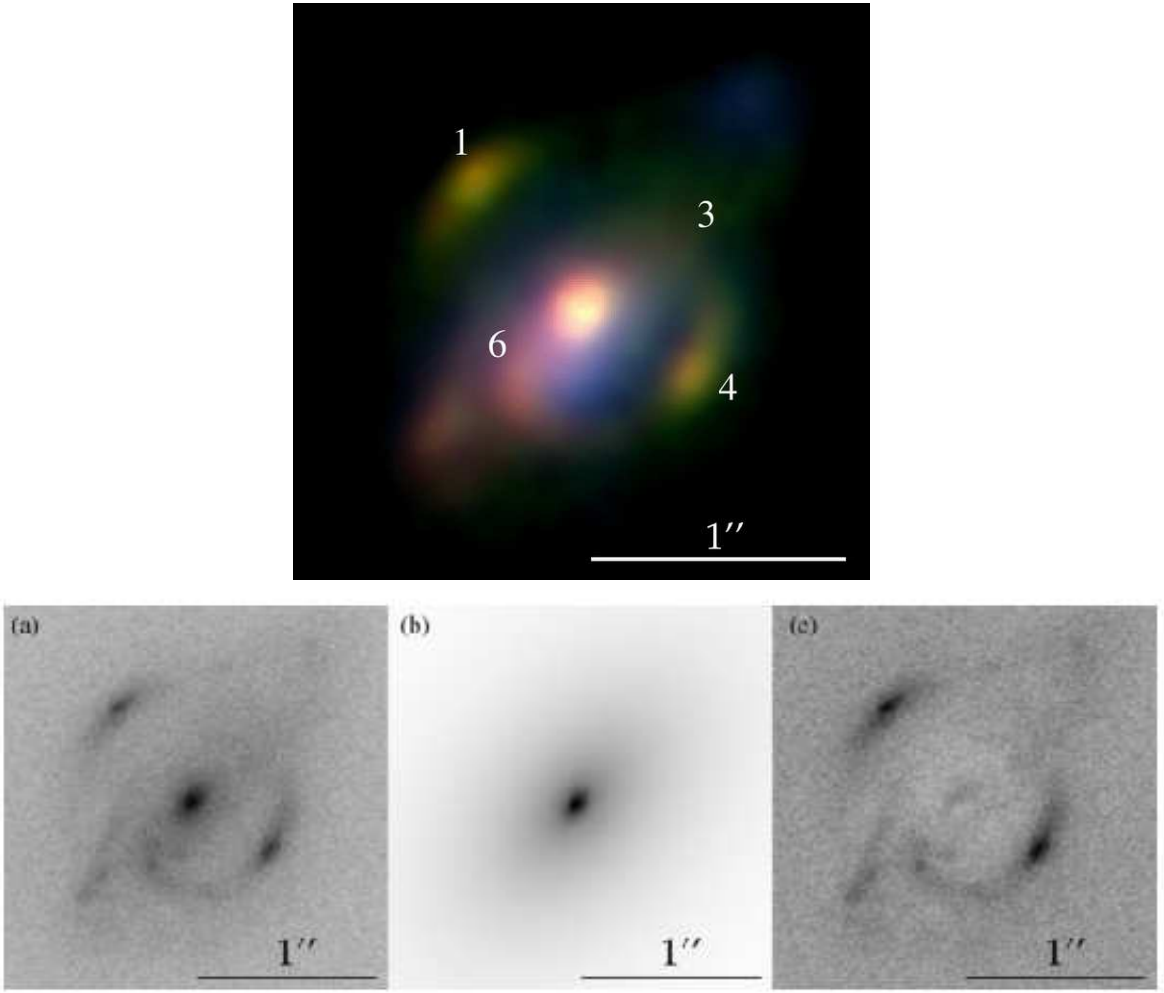

Fig. 4.— From Suyu et al. 2012. Top: an RGB composite of the WFPC2 F814W, NICMOS F160W, and NIRC2 Kp images. The lensed arcs correspond to radio image components 1, 3, 4, and 6 of the compact core. Component 3 is barely visible and component 6 is reddened due to dust extinction in the plane of the spiral galaxy. Bottom, lens galaxy light. (a) NIRC2 Kp image, (b) modeled lens galaxy light based on two exponential disk profiles for the galaxy disk and bulge, (c) residual image.

4. WOULD YOU BUY A LENS?

4.1. A STRONG LENS?

- Using lensing we can obtain estimates of the total mass contents, baryonic plus dark matter from systems at a wide range of cosmological distances. Strong lensing, in particular, provides a wealth of information about the nature of galaxies (see Kochanek 2006 and references therein).

- With typical image separations of 1 arcsec, quasars lensed by single galaxies yield mass estimates near the centers of lens galaxies, constraining both the baryon- dominated luminous core and the inner regions of the dark matter halo. This relatively small angular size (corresponding to physical scales of 5-10 kpc at typical lens-galaxy redshifts) minimizes the probability of foreground objects contaminating the line of sight so that the observed lensing is dominated by the mass of the lens galaxy.

4.2. A RING?

- Kochanek, Keeton & McLeod (2001) showed that when compared with two-image systems, constraints from an Einstein ring break degeneracies between the monopole and higher-order terms of the gravitational potential. Removing these degeneracies yields well-constrained measurements of the slope of the lens galaxy's mass profile and, when combined with time delay information, provides an unambiguous measurement of the Hubble constant (e.g. Suyu et al. 2010).

- Models for Einstein-ring lenses are sensitive to perturbations of the smooth gravitational potential of the

lens galaxy (Vegetti & Koopmans 2009a). Satellite galaxies and dark matter sub-halos that orbit the main lens galaxy can give rise to these perturbations. Although these objects are often too faint to be detected, lensing can be used to detect them indirectly through their perturbations. Thus, Einstein ring lenses are useful to constrain the properties of extragalactic substructure (e.g., Suyu & Halkola 2010). That is also a direct test of the ΛCDM numerical simulations that predict such substructure (e.g., Springel et al. 2008). They help us study the nature of galaxy formation and evolution, as well as the nature of dark matter.

5. THE PLAN

At optical and NIR wavelengths, two techniques yield the data necessary for studies of strong lensing: space-based with HST and ground-based AO imaging.

SHARP (LAG12) hopes to detect and measure the mass of substructures associated with lens galaxies.

Numerical simulations of galaxy formation predict a large amount of substructure for a galaxy-mass halo, with a mass fraction of $f_{\rm sub} = 5 - 10$ % of the total halo mass contained in substructures with masses between 4×10^6 and $4 \times 10^9 \mathcal{M}_\odot$. (e.g., Springel et al. 2008). Furthermore, the simulations converge on a substructure mass function of $dN/dm\ m^\alpha$, where $\alpha = 1.9 \pm 0.1$ (e.g., Diemand, Kuhlen, & Madau 2007). Vegetti & Koopmans (2009b) have shown that a Bayesian analysis of a sample of lenses that have been surveyed for substructure down to some mass threshold can provide meaningful constraints on $f_{\rm sub}$ and the slope of the mass function, α. Given a sample of ~ 30 lens systems, a mass detection threshold of $3 \times 10^8\ \mathcal{M}_\odot$or better, and a reasonable prior on α, strong constraints on $f_{\rm sub}$ are obtained. A non-detection of substructure down to the mass limit provides

useful information for constraining $f_{\rm sub}$ and α, especially as the mass detection limit becomes smaller.

Two complementary methods are available to detect substructure in lens systems. Both require deep, high-resolution imaging. The first is to detect luminous satellites directly, thus fixing the location of the substructure. The substructure can thereafter be included in mass models of the lens and its mass can be determined (e.g., More et al. 2009). This method is most effective for lens systems with either four lensed images or extended lensed emission. The second is to detect substructures through their gravitational effect on extended lensed emission (e.g., Vegetti et al. 2010).

5.1. LAG12 DATA

LAG12 imaged B1938+666 with the NIRC2 camera on the Keck-II telescope, using the Laser Guide Star (LGS) AO system. They used H and K filters.

The reduced images from the LAG12 AO observations are shown in the lower row of Fig. **??**. The images have 3 distinct features: a bright, compact lens galaxy in the center of the image, a well-detected (high SNR) Einstein ring, and faint arcs outside the ring to its East.

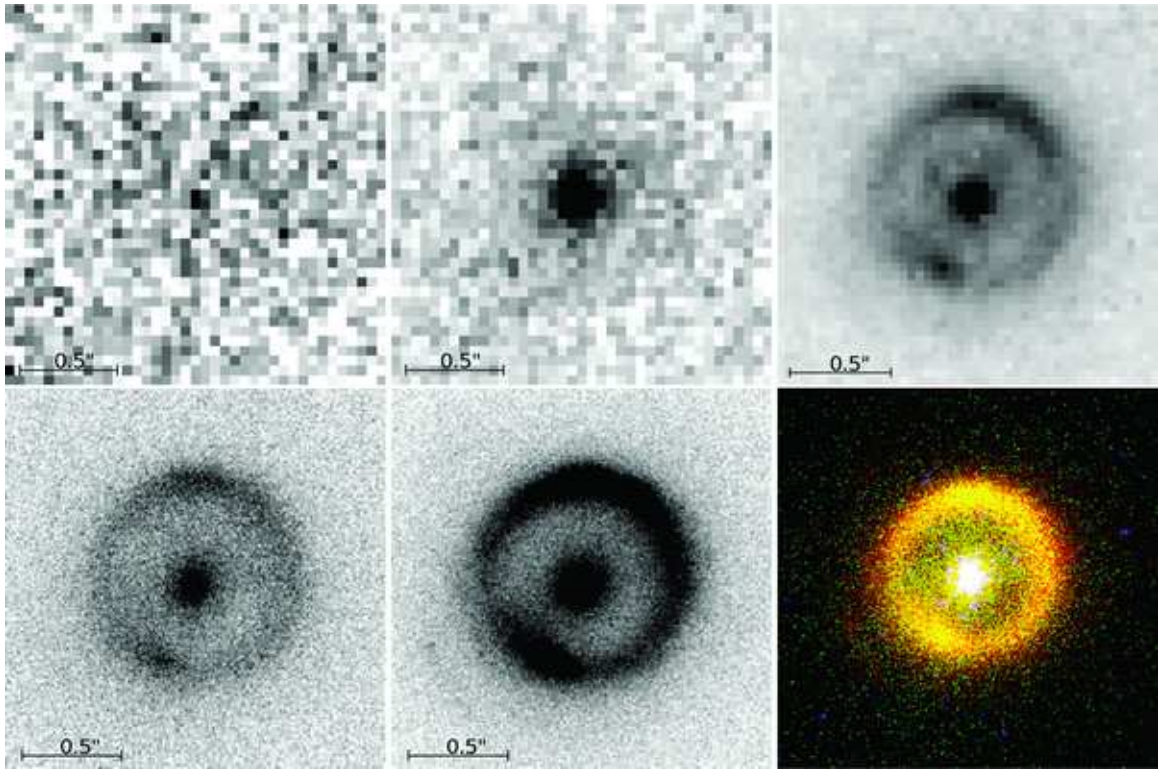

Fig. 5.— Top row: HST images through F555W (V band), F814W (I band) and F160W (H band) filters, respectively, from left to right (CASTLES). Bottom row: Keck II Telescope LGS AO images showing the H-band (left-hand panel) and K-band (middle panel) light. A color composite image (right-hand panel) was made by combining the HST V- and I-band images with the LGS AO H- and K-band images. North is up and East to the left. The lens and source galaxies are clearly seen in all of the NIR bands. A second set of faint arcs can be seen on the eastern side of the K-band image.

6. LENS MODELS

Strong lenses with extended-source structures are frequently modeled by first determining and subtracting the surface brightness distribution of the foreground galaxy (e.g., Bolton et al. 2006). If the background object is very bright, this can lead to an over-subtraction, where parts of the strongly lensed features are fitted and removed along with the foreground galaxy light (e.g. Auger et al. 2011). At NIR wavelengths, the (lensed) source galaxy is roughly equal in brightness to the foreground (lens) galaxy, so the system presents a similar modeling challenge. LAG12 first fitted a simply parametrized lens model to the data to quantify and remove the foreground galaxy light. They then fitted a more detailed lens model to the residual data, to refine the properties of the mass distribution.

6.1. SURFACE BRIGHTNESS MODEL

Modeling the surface brightness distribution for B1938+666 requires an approximate model for the lens mass distribution, to separate the foreground lens and background source light. LAG12 used an elliptical power law mass model (e.g. Barkana 1998) to describe the mass distribution, with an external shear. The foreground and background galaxy surface brightness distributions were modeled with Sérsic (1963) profiles of the form

$$\mu(R) = \mu_e + \frac{2.5b_n}{ln(10)}[(R/R_e)^{1/n} - 1] \quad (1)$$

LAG12 fitted models to the data with an adaptive simulated annealing scheme; each potential model included either a single surface brightness component for both the lens and source galaxies, a single surface brightness component for one galaxy and two components for the other, or two surface brightness components for each galaxy. The foreground galaxy was well-modeled with a single Sérsic component. The background source model strongly favors 2 components. Although LAG12 found significant covariance between the structural properties (i.e., the Sérsic indices n, effective radius R_e, and total magnitudes) of the foreground and background components when fitting to the AO images, the central surface brightness distributions were well separated. For example, the total magnitude of the foreground galaxy could change by 0.5 magnitudes if one or two components were used for the background source, but the flux within the Einstein radius only varied by about 0.1 magnitudes.

According to LAG12, the covariance between the total galaxy properties was due to their inadequate knowledge of the AO PSF. They restricted their discussion of the surface brightness properties to the inferred luminosity within the Einstein radius and the position of the source relative to the lens. The aperture magnitudes within the Einstein radius were then $m_H = 21.0 \pm 0.15$ and $m_K = 20.6 \pm 0.10$.

6.2. MASS MODEL

LAG12 modeled the Keck AO H-and K-band data together with the HST NICMOS F160W-band data with the adaptive and grid-based Bayesian technique of Vegetti & Koopmans (2009a). They modeled the system assuming an elliptical power-law mass density $\rho(r) \propto r^{-\gamma}$ for the lens galaxy, which they use to reconstruct the surface brightness of the source galaxy (after first subtracting the lens galaxy light profile) on a two-dimensional grid. This grid is adaptive in magnification and built by projecting pixels from the image plane to the source plane.

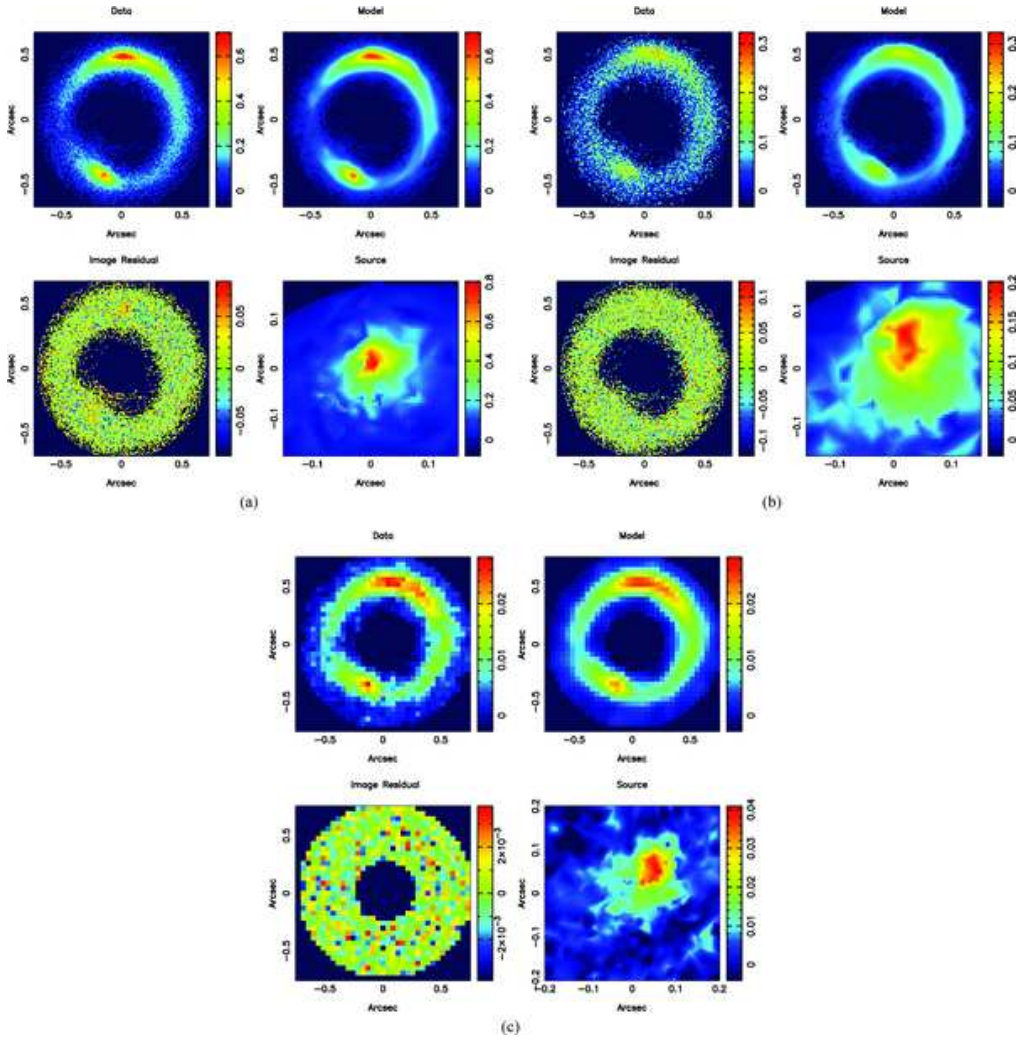

Fig. 6.— Mass model for B1938+666, using the adaptive grid-based method of Vegetti & Koopmans (2009a). Results for the 3 independent data sets: (a) AO K band, (b) AO H band and (c) HST NICMOS H band. Each panel shows the measured surface brightness distribution of the Einstein ring (top-left panel), the best-fitting smooth lens model reconstruction (top-right panel), the residual image (bottom-left panel) and the reconstructed unlensed image of the background source galaxy (bottom-right panel). The source reconstruction grids are not registered. LAG12 find that the source positions are consistent with a single center of brightness, independent of wavelength.

Model	b	θ	q	γ	Γ	Γ_θ	Evidence
M_K	0.452	-22.4	0.853	2.05	0.014	-77.1	
	0.413	-24.3	0.846	2.12	0.013	-72.7	48806
M_H	0.447	-22.3	0.853	2.05	0.019	-78.5	
	0.410	-28.5	0.786	2.12	0.029	-89.1	46280
M_{HST}	0.439	-23.0	0.856	2.07	0.016	-74.1	
	0.424	-25.0	0.918	2.09	0.031	-42.4	7027

Table 1: Extract from Table 2 of LAG12. Parameters of the grid-based reconstruction lens models. The first row of each model (first column) is the maximum-likelihood model solution; the second row shows the mean values for each parameter's posterior probability distribution. The model parameters are b, the model lens strength in arcsec; θ, the position angle of the mass distribution of the lens galaxy (deg E of N); q, the axis ratio; γ, the power-law slope of the mass profile; Γ and Γ_θ the magnitude and position angle of an external shear. The global Bayesian evidence of each model is in the last column.

The best lens models (from a maximum-likelihood analysis) for the K-band, H-band, and NICMOS data are shown in Figs. 6(a), 6(b) and 6(c), respectively. The parameter values for these models are listed in the Table. In addition to the maximum-likelihood values, LAG12 derived mean values and confidence intervals for each parameter's marginalized posterior probability distribution function by exploring the Bayesian evidence in the full multidimensional parameter space (see the Table for a sample of results). One-and two-dimensional slices of these marginalized posterior probability distributions are shown in Fig. 7. Using Multi-nest v2.7 (Feroz & Hobson 2008), LAG12 integrated over this posterior probability to obtain the marginalized Bayesian evidence, the probability of the data given each model family.

Incorporating a robust PSF model can be challenging for AO data, as the PSF varies rapidly over time. This is a particular concern for the B1938+666 AO data as LAG12 was unable to observe the lens system and a PSF star simultaneously. Therefore, they conduct the modeling with different PSF stars observed at different times, leading to a different "best" model for each PSF. As the arc is sufficiently extended and the dynamic range is relatively low, LAG12 found that the lens modeling is not significantly affected by the choice of PSF (Vegetti et al. 2012). However, the Bayesian evidence allows one to choose the best PSF model objectively. For example, for the PSF used in the model labeled M_K in the table, the largest evidence was found for the K-band data.

The best models for each data set are consistent, as we see in the table. Many of the marginalized posterior probability distributions are also in agreement (Fig. 7), although there were some discrepancies in the axis ratios and external shear parameters, especially between the NICMOS and H-band models. However, the precision with which the lens parameters can be recovered is significantly higher for the Keck AO data, with the highest precision obtained for the K-Band. Thus, the higher resolution provided by the AO imaging leads to more precise lens models, when compared to the HST imaging, despite the lower signal-to-noise ratio (SNR) for AO. All the models that use the adaptive and grid-based Bayesian technique lead to a total mass centroid position and flattening that are consistent with those of the parametric mass modeling presented. Also, all the models have a total density profile that is very nearly isothermal (i.e., $\gamma = 2$) out to the Einstein radius of the system.

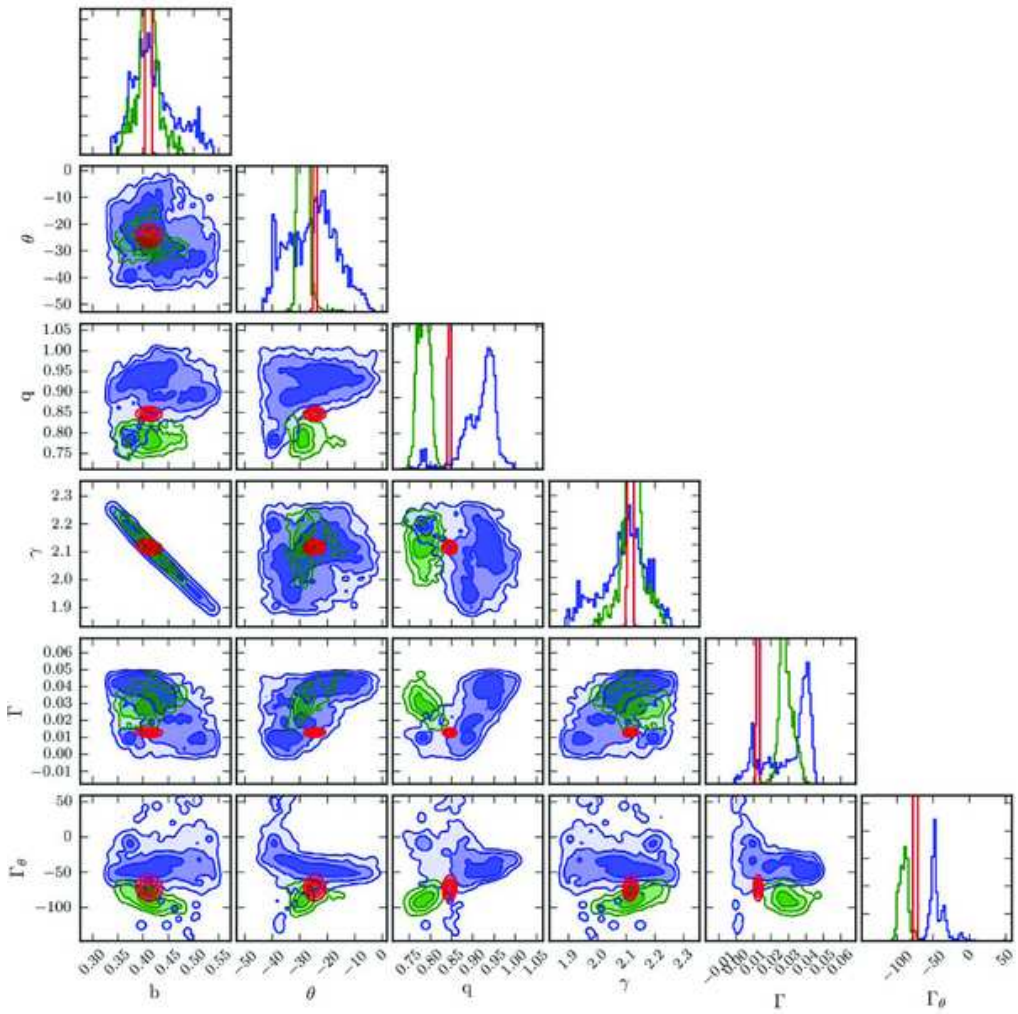

Fig. 7.— Marginalized posterior probability distributions of the lens model parameters, as measured by a nested sampling analysis. Each grid shows a different marginalization: the two-dimensional contours represent the distribution between two model parameters (specified by the row and column), while the one-dimensional histograms at the top of each column represent the distribution of a single parameter. The AO K band, AO H band and NICMOS data are represented by red, green and blue contours, respectively. The maximum-likelihood model values for each parameter, and their uncertainties, are presented in the table.

7. COMPARING HST and AO

The precision and accuracy of mass model constraints from extended sources on strong gravitational lens galaxies is set by three conditions:

1. the number of independent resolution elements across the lensed images (and their multiplicity),
2. the SNR of the lensed-image surface brightness distribution and
3. the SNR of surface brightness structure in the lensed source.

The first two conditions set the information content in the lensed images and how well the mass model of the lens galaxy can be constrained. The third determines the level of covariance (i.e., degeneracy) in the mass model, where more structured sources lead to less covariance between model parameters. One of the goals of LAG12 was to illustrate these effects by comparing the results of high SNR HST F160W-band data with both lower resolution and pixel- sampling, and lower SNR Keck AO imaging data with higher resolution and sampling.

Although the results of the modeling of the 3 very different data sets are very similar and the errors are small, there are differences. There are discrepancies between the axis ratio and position angle (PA) of the lens mass distribution, and the external shear strength and PA (see the Table). These quantities are strongly covariant (e.g., the external shear mimics the flattening of the lens potential/mass-distribution) and lack of information combined with noise results in biases in the maximum-likelihood solutions and the posterior probability distributions of individual parameters. This is especially true here, where a nearly circular mass distribution and featureless Einstein ring add uncertainty to the lens model. Specifically, the circularly symmetric mass distribution (coupled

with nearly coaxial foreground and background galaxies) makes it difficult to constrain the lens galaxy's mass slope while the smooth light distribution lacks the contrast needed to differentiate between small-scale variations on the model. Thus, even moderate variations in parameter space can leave the lensed light distribution relatively unchanged, allowing significantly different models to fit the data equally well.

The marginalized probability distributions in Fig 7 show that there is a strong correlation between the lens strength b and mass slope γ, especially in the H-band and NICMOS models. This is why model discrepancies are the strongest between these data sets. However, these degeneracies, and the parameter uncertainties in general, are much smaller from the higher-resolution (but lower SNR) Keck AO data. This implies that at least for some systems, ground-based AO data can outperform space-based data in precision due to the better sampling of the image structure. Of course, high SNR data remains necessary: of the two AO-based models, the K-band data (with its relatively higher SNR) provides much tighter constraints on individual parameters than the H-band model, and even breaks the mass-slope degeneracy found in the H-band and NICMOS models. The comparison shows that between SNR and image resolution, resolution dominates any limitations on model precision.

One cannot generalize this conclusion to other lens systems, because the result depends critically on the interplay between SNR, spatial resolution, and source structure. It could be that lens systems with highly-structured sources (e.g., space-based B-or U- band data, where star formation could be strong and the sources could be more structured) could out-perform the higher resolution K-band AO data. In cases where there are similar data, and a bright star is available, however, the LAG12 results show that ground-based AO data can perform significantly better than HST data in constraining lens models.

8. LENS GALAXY

The lens galaxy is clearly seen in the optical and NIR data sets (Fig. 2). Its surface brightness distribution is well-modeled by a single elliptical Sérsic profile. The galaxy has colors I-H= 1.9 mag and H-K= 0.4 mag, after Galactic reddening corrections. LAG12 model these colors with the Bruzual & Charlot (2003) stellar population code and, assuming a Solar metallicity and no dust, find consistency with an old (> 4 Gyr) stellar population. The foreground galaxy's isophotal regularity, colors, and absorption line spectrum measured by Tonry & Kochanek (2000) suggest an early-type morphology.

LAG12 used the Bruzual & Charlot (2003) 4-Gyr stellar population model to compute the V-band absolute magnitude and to estimate the stellar mass within the Einstein radius. They found $L_V = 3 \times 10^{10}\ \mathcal{L}_\odot$. The stellar template has a V-band stellar mass-to-light ratio of 1.54, implying a stellar mass within the Einstein radius of $M_* = 4.7 \times 10^{10}\ \mathcal{M}_\odot$for a Chabrier initial mass function (IMF) and a dark-matter mass fraction $M_{dark}/M_{lens} = 0.55$ within the Einstein radius. For a Salpeter IMF, the stellar mass within the Einstein radius is $M_* = 8.2^{10}\ \mathcal{M}_\odot$, and a dark-matter mass fraction of $M_{dark}/M_{lens} = 0.2$.

It is necessary to compute the stellar-to-total mass fraction within an aperture that is physically associated with the lens galaxy. LAG12 used two methods to estimate the effective radius. First, they used the relationship between the power-law density slope and effective radius found by Auger et al. (2010) and corrected for early-type galaxy growth rates. With caveats such as evolution of the power-law slope (e.g., Bolton et al. 2012) and large uncertainties on these relationships, they find that the effective radius is consistent with the size of the Einstein radius.

LAG12 checked whether an effective radius of $0\farcs45$ (i.e., equivalent to the Einstein radius) is consistent with

measurements of the fundamental plane. They used the velocity dispersion inferred from the lens model as an estimate of the stellar velocity dispersion and applied a passive evolution correction to the luminosity as determined by the Bruzual & Charlot (2003) 4 Gyr template. They found that, correcting for size evolution, their assumption that the effective radius is equal to the Einstein radius is consistent with the fundamental plane in Auger et al. (2010).

9. MAGNIFICATION OF LENSED NIR

The lens models provide an estimate of the source surface brightness distribution, after correcting for the lens magnification. From the pixelated reconstruction, LAG12 find that the source has 2 components at NIR wavelengths (in agreement with the parametrized source distribution). One component is a high surface brightness region with a projected size of ~ 0.8 kpc; the size of the second one is ~ 1.6 kpc with a lower surface brightness.

To estimate the total magnification of the NIR source from the lens models, LAG12 compared the images with the reconstructed sources. They found the total magnification factor of the NIR emission is ~ 13. A magnification of 176 was previously reported for B1938+666 from a simple point-source model (Barvainis & Ivison 2002). This magnification was used by Riechers (2011) for their analysis of the molecular gas properties of B1938+666; they found that the CO $(3-2)$ line intensity, and hence the molecular gas mass, was about an order of magnitude lower than for other quasars at a similar epoch. This is due to the over-estimated magnification of the gas emission.

10. SUBSTRUCTURE

Vegetti et al. (2012) presented the detection of a low-mass substructure in the B1938+666 system from the effects of substructure on the lensed arc. LAG12 find no evidence of any luminous,substructure in the residual images for the system. To determine an upper limit on the brightness of any luminous substructure, LAG12 added a series of simulated point sources with $24.5 < m_{\rm K} < 28$ to an image of the lens system with both the lens galaxy and the Einstein ring subtracted. For their point source model, they chose the empirical PSF star used in the lens modeling. One example simulation is shown in Fig. 8. LAG12 chose point sources for simplicity.

LAG12 generated 1000 simulated images, randomizing both the magnitudes and positions of the point sources, and then used SExtractor to find the added satellites. A point source is detected if SExtractor finds an object within 5 pixels and 1.5 magnitudes of the actual position and magnitude of each simulated object. Compiling the results into magnitude bins, they found they recovered the majority (i.e. over 50%) of the simulated objects down to an apparent magnitude of K= 26.1. They use that value as their detection limit (see Fig. 9). Converting it to the rest-frame V band corresponds to an object that has an absolute magnitude of $M_{\rm V} = 16.2$, fainter than the Magellanic clouds ($M_{\rm V,LMC} = -18.5$, $M_{\rm V,SMC} = -17.1$) but approximately three times brighter than the Sagittarius dwarf satellite ($M_{\rm V,Sgr} = -15$; Tollerud et al. 2008).

11. MORE LENSED OBJECTS?

There are 2 faint arclets just outside the Einstein ring on the east side of the K-band image (Fig. 3; bottom middle panel). To enhance these arclets, LAG12 applied a Gaussian filter ($\sigma = 6.5$ pixels) to smooth the data, followed by a Laplacian filter to increase the contrast of bright flux peaks. Fig. 10 shows a high-contrast image of the original data and an image showing the results of the filters. The two arcs are barely detectable above the noise in the unfiltered data, but they are clearly visible in the filtered image. As the arclets are so faint in the original K-band data, they cannot constrain the lens model. However, the filtered image indicates that the arclets may well be multiple images of a second background source.

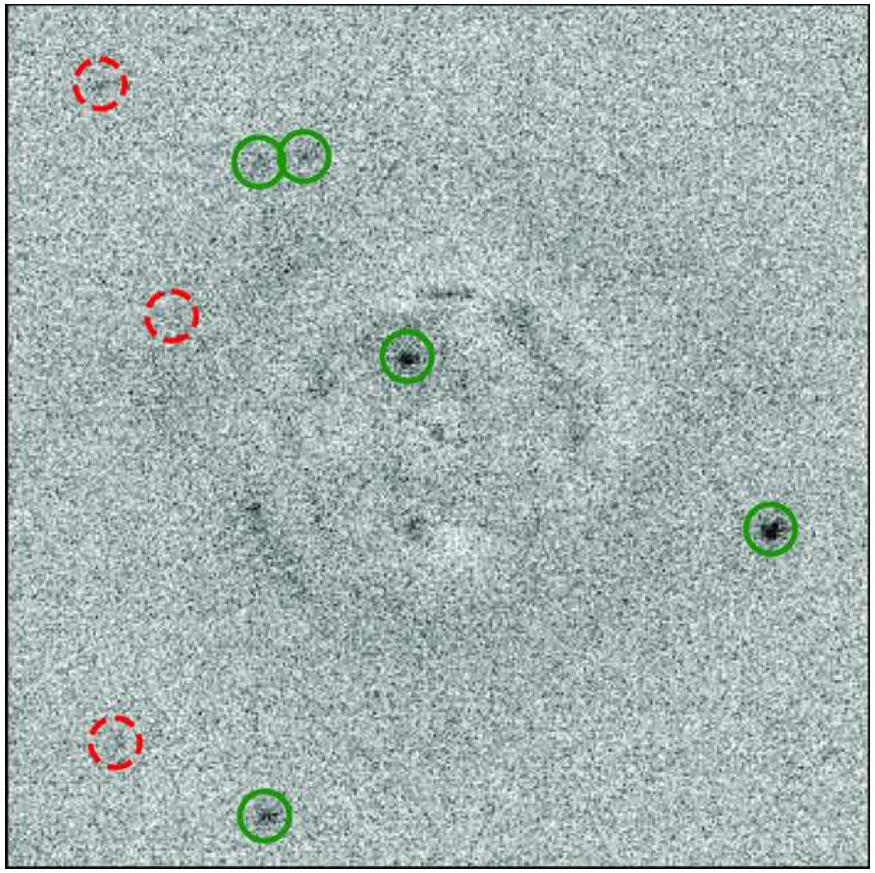

Fig. 8.— Residual image with simulated point-source objects added, which LAG12 used to estimate a detection limit for luminous substructure. The point sources detected by SExtractor are green, solid-line circles, while those that are missed are represented by red, dashed circles. There is a distinct difference in noise level between the regions inside and outside of the Einstein ring, suggesting that the substructure limiting magnitude should be brighter closer to the lens.

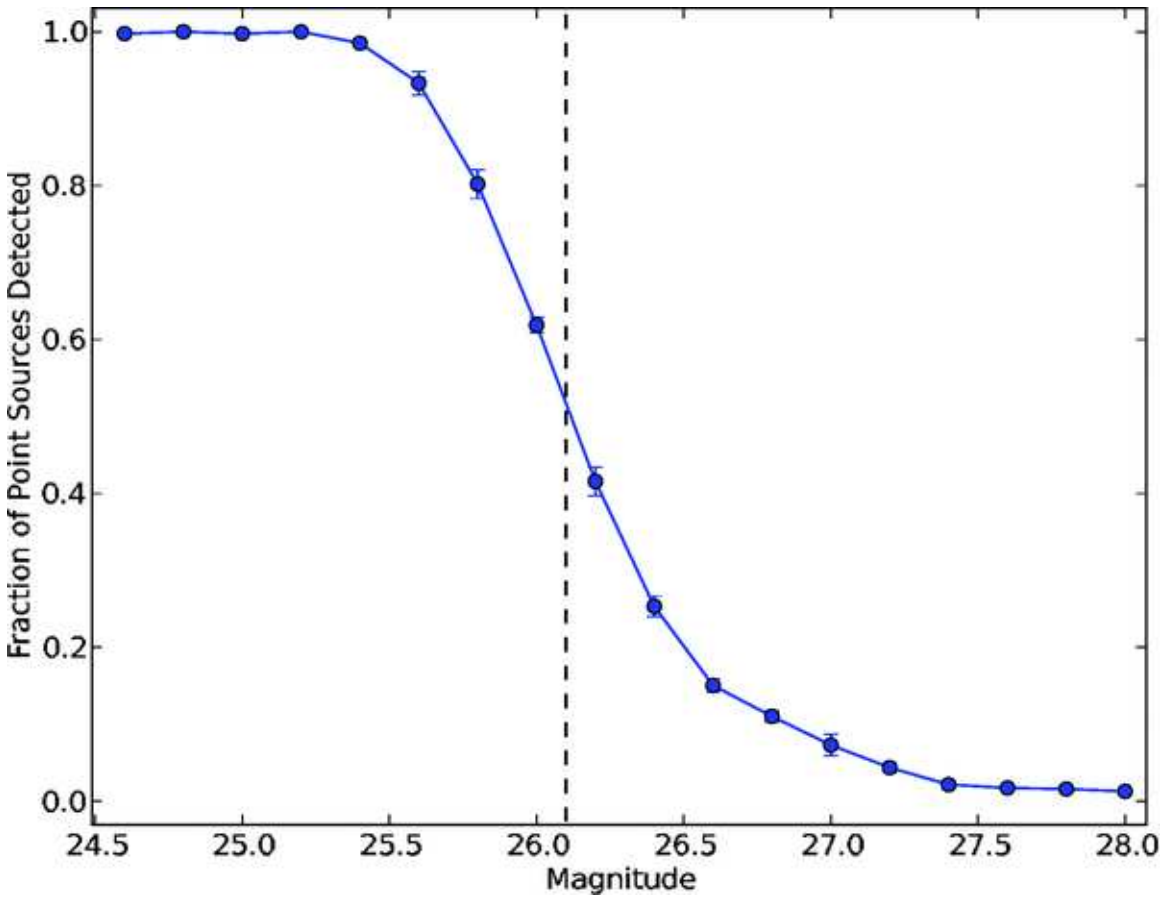

Fig. 9.— Fraction of simulated point sources recovered by SExtractor, binned as a function of magnitude. Over 50% are recovered in each magnitude bin, up to and including the $m_K = 26.1$ bin (dashed line). LAG12 deduced this value was their limiting magnitude.

There are 3 possible scenarios for the arclets:

1. They are not lensed.

2. They are images of a strongly-lensed source associated with the primary ring (e.g., an additional component of the galaxy lensed into the ring, a nearby galaxy, or more images of the ring, although this would lead to a peculiar image configuration. LAG12 used their best lens model to project the Einstein ring and the two arclets onto the source plane. The arclets did not map to the source of the Einstein ring. The two arclets are also **not** mapped to a single location on the source plane, indicating that if they are at the same redshift as the Einstein ring galaxy they are not multiple images of the same source.

3. They are images of a second source that is strongly lensed but lies at a redshift other than z_l. Such double-plane lens systems provide very tight constraints to the mass-density slope of the lens and can set useful constraints on cosmological parameters (e.g., Gavazzi et al. 2008). LAG12 rescaled the lens strength of their mass model, where the scaling is directly proportional to the ratio of angular diameter distances between the lens and the two sources. The arclets were then mapped to a single source if the lens strength was increased by a factor of ~ 1.85. Such a large factor requires an unrealistically high redshift for the source. However, the galaxy being lensed into the Einstein ring may contribute to the lensing, and the mass profile could deviate from the central power law of the Einstein-ring fit.

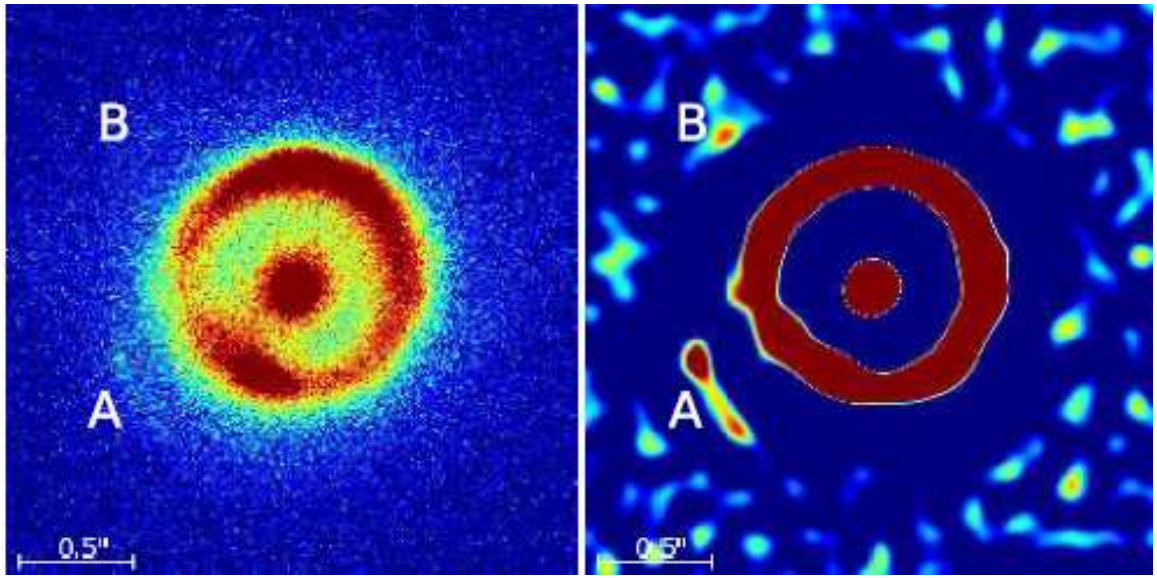

Fig. 10.— Left: K-band image of B1938+666 with the two arclets hightlighted (A and B). Right: same image after applying a Gaussian filter, and then a Laplacian filter to sharpen faint features.

Measurements of the redshifts of the arclets could settle these questions. That requires deep, high-resolution spectroscopy beyond the capabilities of current telescopes. The James Webb Space Telescope (JWST), the Giant Magellan Telescope (GMT), or the European-Extremely Large Telescope (E-ELT) would provide the required resolution and light-gathering power.

REFERENCES

Auger M. W., Treu T., Bolton A. S., Gavazzi R., Koopmans L. V. E., Marshall P. J., Bundy K., Moustakas L. A., 2009, ApJ, 705, 1099

Auger M. W., Treu T., Gavazzi R., Bolton A. S., Koopmans L. V. E., Marshall P. J., 2010, ApJ, 721, L163 Auger M. W., Treu T., Brewer B. J., Marshall P. J., 2011, MNRAS, 411, L6

Barkana R., 1998, ApJ, 502, 531

Barvainis R., Ivison R., 2002, ApJ, 571, 712

Behroozi P. S., Conroy C., Wechsler R. H., 2010, ApJ, 717, 379

Bertin E., Arnouts S., 1996, A&AS, 117, 393

Blumenthal G. R., Faber S. M., Flores R., Primack J. R., 1986, ApJ, 301, 27

Bolton A. S., Burles S., Koopmans L. V. E., Treu T., Moustakas L. A., 2006, ApJ, 638, 703

Bolton A. S. et al., 2012, ApJL, submitted (arXiv:1201.2988)

Bosma A., 1999, ASPC, 182, 339

Browne I. W. A., Wilkinson P. N., Patnaik A. R., Wrobel J. M., 1998, MNRAS, 293, 257

Bruzual G., Charlot S., 2003, MNRAS, 344, 1000

Conroy C. et al., 2007, ApJ, 654, 153

de Blok W. J. G., McGaugh S. S., 1997, MNRAS, 290, 533

Diemand J., Kuhlen M., Madau P., 2007, ApJ, 667, 859

Diemand J., Kuhlen M., Madau P., Zemp M., Moore B., Potter D., Stadel J., 2008, Nat, 454, 735

Dutton A. A., et al., 2011, MNRAS, 417, 1621

Feroz F., Hobson M. P., 2008, MNRAS, 384, 449

Fukugita M., Hogan C. J., Peebles P. J. E., 1998, ApJ, 503, 518

Gavazzi R., Treu T., Rhodes J. D., Koopmans L. V. E., Bolton A. S., Burles S., Massey R. J., Moustakas L. A., 2007, ApJ, 667, 176

Gavazzi R., Treu T., Koopmans L. V. E., Bolton A. S., Moustakas L. A., Burles S., Marshall P. J., 2008, ApJ, 677, 1046 Gnedin O. Y., Kravtsov A. V., Klypin A. A., Nagai D., 2004, ApJ, 616, 16

Heymans C. et al., 2006, MNRAS, 371, L60

Hoekstra H., Yee H. K. C., Gladders M. D., 2004, ApJ, 606, 67

King L. J., Browne I. W. A., Muxlow T. W. B., Narasimha D.,

Patnaik A. R., Porcas R. W., Wilkinson P. N., 1997, MNRAS, 289, 450

King L. J. et al., 1998, MNRAS, 295, L41

Kochanek C. S., 2006, glsw.conf, 91

Kochanek C. S., Keeton C. R., McLeod B. A., 2001, ApJ, 547, 50

Koopmans L. V. E., 2005, MNRAS, 363, 1136

Lagattuta D. J. et al., 2010, ApJ, 716, 1579

Lagattuta D. J., Auger M. W., Fassnacht C. D., 2010, ApJ, 716, L185

Mandelbaum R., Seljak U., Kauffmann G., Hirata C. M.,

Brinkmann J., 2006, MNRAS, 368, 715

McKean J. P. et al., 2007, MNRAS, 378, 109

More A., McKean J. P., More S., Porcas R. W., Koopmans L. V. E., Garrett M. A., 2009, MNRAS, 394, 174

McLean I. S., et al., 1998, SPIE, 3354, 566

Napolitano N. R., Romanowsky A. J., Tortora C., 2010, MNRAS, 405, 2351

Newman A. B., Ellis R. S., Treu T., Bundy K., 2010, ApJ, 717, L103

Patnaik A. R., Browne I. W. A., Wilkinson P. N., Wrobel J. M., 1992, MNRAS, 254, 655

Riechers D. A., 2011, ApJ, 730, 108

Rhoads J. E., Malhotra S., Kundic T., 1996, AJ, 111, 642

Rubin V. C., Peterson C. J., Ford W. K. Jr., 1980, ApJ, 239, 50

Ruff A. J., Gavazzi R., Marshall P. J., Treu T., Auger M. W., Brault F., 2011, ApJ, 727, 96

Schulz A. E., Mandelbaum R., Padmanabhan N., 2010, MNRAS, 408, 1463

Sérsic J. L., 1963, BAAA, 6, 41

Springel V. et al., 2008, MNRAS, 391, 1685

Suyu S. H., Halkola A., 2010, A&A, 524, A94

Suyu S. H., Marshall P. J., Auger M. W., Hilbert S., Blandford R. D., Koopmans L. V. E., Fassnacht C. D., Treu T., 2010, MNRAS, 711, 201

Suyu S. H., et al., 2012, ApJ, 750, 10

Tollerud E. J., Bullock J. S., Strigari L. E., Willman B., 2008, ApJ, 688, 277

Tonry J. L., Kochanek C. S., 2000, AJ, 119, 1078

van Albada T. S., Sancisi R., 1986, RSPTA, 320, 447

Vegetti S., Koopmans L. V. E., 2009a, MNRAS, 392, 945

Vegetti S., Koopmans L. V. E., 2009b, MNRAS, 400, 1583

Vegetti S., Czoske O., Koopmans L. V. E., 2010, MNRAS, 407,

225

Vegetti S., Koopmans L. V. E., Bolton A., Treu T., Gavazzi R., 2010, MNRAS, 408, 1969

Vegetti S., Lagattuta D. J., McKean J. P., Auger M. W., Fassnacht C. D., Koopmans L. V. E., 2012, Nat, 481, 341

Wilkinson P. N., Browne I. W. A., Patnaik A. R., Wrobel J. M., Sorathia B., 1998, MNRAS, 300, 790